

Article

Copper Oxide Nitrogen-Rich Porous Carbon Network Boosts High-Performance Supercapacitors

Dan Li ^{1,2}, Hanhao Liu ^{1,2} , Zijie Liu ^{1,2}, Que Huang ^{2,*} , Beihu Lu ^{3,*}, Yanzhong Wang ^{1,2}, Chao Wang ^{1,2} and Li Guo ²

¹ School of Materials Science and Engineering, North University of China, Taiyuan 030051, China; lidan@nuc.edu.cn (D.L.); liuhanhao100@163.com (H.L.); liuchuangliuzijie@163.com (Z.L.); wyzletter@nuc.edu.cn (Y.W.); wangchao_nuc@126.com (C.W.)

² Advanced Energy Materials and Systems Institute, North University of China, Taiyuan 030051, China; guoli@nuc.edu.cn

³ Wuhan Institute of Marine Electric Propulsion, Wuhan 430060, China

* Correspondence: que.huang@nuc.edu.cn (Q.H.); lufangzhi624@163.com (B.L.)

Abstract: Transition metal oxides with various valence states have high specific capacitance and have attracted much attention. However, the poor cycle stability caused by material agglomeration seriously limits the play of its high activity. Herein, we create a stress dispersion structure (Cu_xO composite porous carbon net) by in situ lyophilization and one-step carbonization, effectively anchoring highly reactive copper oxides and highly conductive carbon networks combined with high nitrogen doping of 10.7%, to investigate their electrochemical performance in supercapacitors. Specifically, the specific capacitance of Cu_xO@NPC can be as high as 392 F/g (0.5 A/g) in the three-electrode system with 6 mol/L KOH as electrolyte. When applied to the two-electrode system, the cycle stability of the whole device can reach 97% after 10,000 cycles.

Keywords: copper; carbon network; porous; supercapacitors



Citation: Li, D.; Liu, H.; Liu, Z.; Huang, Q.; Lu, B.; Wang, Y.; Wang, C.; Guo, L. Copper Oxide Nitrogen-Rich Porous Carbon Network Boosts High-Performance Supercapacitors. *Metals* **2023**, *13*, 981. <https://doi.org/10.3390/met13050981>

Academic Editor: Gabriele Mulas

Received: 30 March 2023

Revised: 8 May 2023

Accepted: 14 May 2023

Published: 19 May 2023



Copyright: © 2023 by the authors. Licensee MDPI, Basel, Switzerland. This article is an open access article distributed under the terms and conditions of the Creative Commons Attribution (CC BY) license (<https://creativecommons.org/licenses/by/4.0/>).

1. Introduction

Given the vast usage of nonrenewable energy, the growing urgency of environmental conservation on earth compels academics to create clean and sustainable energy sources such as solar, wind, and electric energy [1,2]. However, these renewable energy sources have disadvantages such as intermittency and geographical dependence [3,4]. Therefore, it has become an important task for researchers to develop efficient energy storage devices to utilize renewable energy effectively. At present, some green energy storage devices, such as secondary ion batteries, supercapacitors, fuel cells, and so on, have been widely studied and applied [5,6]. Due to their advantages of high rate capability, a wide working temperature area, and excellent stability, supercapacitors have been widely used in quality energy storage fields. It is known that electrode material is the key factor determining the performance of a supercapacitor [7–9]. The electrode materials for supercapacitors mainly include the following categories [10]: 1. conductive polymers; 2. carbon materials; and 3. transition metal compounds. Carbon materials have the advantages of a large surface area, high chemical stability, and electronic conductivity [11–14]. However, due to their low electrochemical activity, carbon-based symmetric ultracapacitors have lower capacitance and energy density. On the contrary, transition metal compounds with multiple valence states have high specific capacitance and are promising electrode materials. However, their low stability and poor conductivity prevent them from being used in high-performance supercapacitors. Therefore, using the high activity of metal compounds and the high conductivity of carbon-based materials to prepare composite materials, which have a synergistic effect, is an effective measure to prepare high-performance capacitor electrode

materials. The highly conductive substrate also makes it possible to omit the conductive agent required for electrode preparation [15,16].

A lot of reports have proven that the preparation of porous electrode materials can effectively improve the electrochemical active sites on the electrode surface, and the abundant voids in the electrode can provide a large number of rapid diffusion channels for ions. Large pores of porous carbon materials can serve as ion buffer devices to store electrolytes; medium pores can quickly distribute electrolyte ions; and micropores can improve specific capacitance [17,18]. Porous materials are widely used in lithium-ion batteries, sodium-ion batteries, and supercapacitors. Carbon materials with abundant pore structure and high specific surface area are expected to become high-performance electrode materials for supercapacitors [19]. As a transition metal, copper has the advantages of good conductivity, stable chemical properties, abundant resources, and a friendly environment. Polyvalent copper base oxide is a promising electrode material because of its high theoretical specific capacity. However, the conductivity of copper-based oxides is very low. At the same time, the bulk expansion and contraction of copper-based electrode materials occur due to the embedding and removal of ions in the electrochemical charge-discharge process. Its stable nanostructure will crack and fracture with repeated volume changes and eventually collapse [20–22]. In view of this, the researchers proposed to introduce carbon material to buffer the volume strain of copper-based oxide, maintain its structural stability, improve the overall conductivity of the material, and thus improve its capacitor performance. However, preparing carbon and copper-based oxide composites will reduce the vibrational density and energy density of the materials, which is not conducive to the small-scale application of energy storage devices. Therefore, in addition to improving the conductivity, increasing the vibrational density of the material and obtaining an electrode material with a high energy density are also key factors worth considering. It has been reported that, in addition to introducing carbon materials to improve electrical conductivity and buffer volume changes, the introduction of elemental copper into composites can further improve the electrical conductivity of the materials. At the same time, the atomic mass of copper is much higher than that of carbon, so the introduction of simple copper can effectively improve the overall density of the composite material, thus improving the mass energy density [23,24]. Cu-C nanocomposites synthesized by Wang et al. [25] have exhibited a high specific capacitance of 318 F/g at 1 A/g and maintain an ultra-stable cyclic performance during 10,000 cycles. Sirisomboonchai et al. reported that Cu/C composite materials have a specific capacitance of 316.2 F/g at 0.5 A/g. In addition, they found that the introduction of Cu effectively improved the electrochemical performance, which was more than 30 times higher than that without Cu [26]. The NHPC-1 electrode prepared by Zhou et al. possesses a high specific capacitance of 231 F/g at 1 A/g [27]. This indicates that copper oxide composite carbon material has good performance as a supercapacitor. However, the preparation of carbon material and the secondary introduction of copper elements are extremely complicated. During the preparation of electrode paste, additional conductors (Super P) and binders (Sodium carboxymethyl cellulose, $C_8H_{11}O_5Na$) need to be added, which will increase the cost of electrode material and not be conducive to large-scale development.

Based on the above considerations, we prepared Cu_xO composite N-doped porous carbon mesh ($Cu_xO@NPC$) using glucose as a carbon source, copper oxalate as a copper source, and NaCl as a template by in situ solution drying and one-step carbonization. Ultra-high nitrogen doping of 10.7% can greatly increase the electrochemical active sites, and the abundant pore structure in the carbon mesh greatly enhances the ion diffusion, improves the conductivity of the matrix materials, and increases the active ion storage sites. The introduction of copper oxide not only increases electrochemical activity but also enhances electrical conductivity. Thanks to the excellent electrical conductivity of the composite structure, no additional conductive material is required when $Cu_xO@NPC$ is used as the electrode material for supercapacitors. Specifically, when $Cu_xO@NPC$ is applied to a three-electrode system, a high specific capacitance of 392 F/g at 0.5 A/g can be achieved. When applied to the two-electrode system, the cycle stability of the whole device

can reach 97% after 10,000 cycles. This approach is applicable to the creation of different metal oxide composite carbon networks in general and effectively.

2. Experimental Section

2.1. Experimental Procedure

To synthesize an N-doped porous carbon network (NPC), 10 g NaCl, 0.6 g glucose powder, and 0.25 mmol copper oxalate were mixed in 30 mL deionized water and stirred for 3 h. The mixed solution is freeze-dried to obtain a mixed powder, which is then mixed with 0.6 g of urea. The pre-mixed sample was carbonized for three hours at a temperature of 700 °C with a heating rate of 3 °C/min and nitrogen in the environment. To remove NaCl, the resulting black powder was washed with deionized water several times and dried overnight. Finally, Cu composite N-doped porous carbon was obtained ($\text{Cu}_x\text{O@NPC}$). As a comparison, N-doped porous carbon was prepared in the same process as $\text{Cu}_x\text{O@NPC}$ but without the addition of copper oxalate to the initial feedstock, which is named NPC.

2.2. Characterization

The microscopic morphology, microstructure, and element distribution of the obtained samples are visually demonstrated by SEM (HITACHI SU8010, HITACHI, Tokyo, Japan) and TEM (JEOL JEM-F200, JEOL, Tokyo, Japan). The crystal structure and composition of the materials were characterized by XRD in the range of 10–80° with a scanning rate of 5°/min (Empyrean). Synchronous thermal analysis (TG) is performed in an air atmosphere heated from room temperature to 800 °C at a rate of 10 °C/min on a NETASCH STA 449F3 (Netzsch, Bavaria, Germany). The elemental content analysis was obtained by an oxygen, nitrogen, and hydrogen analyzer (ONH836, LECO, St. Joseph, MI, USA). The pore size distribution and specific surface area of carbon mesh were carried out on a Micromeritics ASAP 2020c volumetric adsorption analyzer (Micromeritics, Norcross, GA, USA). The surface chemical state analysis and chemical bond characterization of materials are performed by XPS (Thermo ESCALAB 250XI, Thermo Fisher, Waltham, MA, USA).

2.3. Electrochemical Measurement

In the three-electrode system, Hg/HgO was selected as the reference electrode, and platinum was selected as the counter electrode. As for the working electrode, the active substance and binder were evenly coated on the surface of nickel mesh according to a mass ratio of 85:15. The load of the current collection is controlled at 2.0–2.5 mg/cm². Following that, the nickel foam loaded with the active substance was pressed into a sheet at a pressure of 5 MPa and dried in an oven at 60 °C for 12 h under vacuum. In a two-electrode system, the battery symmetry device consists of two working electrodes. The electrolytic liquid system used for both of them is a 6.0 mol/L KOH aqueous solution. The electrochemical test consists of GCD (galvanostatic charge-discharge), CV (cyclic voltammetry), and EIS (electrochemical impedance spectroscopy), which are used to characterize the specific capacitance, rate performance, ion diffusion resistance, and other related parameters, respectively, and are mainly completed by the LAND test system (CT2001A, LANHE, Wuhan, China) and electrochemical workstation (PGSTAT302N-type, Metrohm, Herisau, Switzerland). The working voltage window is controlled between 0.0 V and 1.0 V.

3. Results and Discussions

Figure 1 shows the preparation process for $\text{Cu}_x\text{O@NPC}$ composite material. Firstly, glucose, NaCl, and copper oxalate were mixed evenly by simple dissolution and agitation, then freeze-dried to obtain hybrid precursor powder. The carbonized glucose and copper oxalate grew and bonded along the NaCl crystal template after being carbonized at 700 °C in a nitrogen atmosphere. After carbonization, NaCl was removed by washing, and a three-dimensional network structure was finally formed. The micromorphology of NPC and $\text{Cu}_x\text{O@NPC}$ is characterized by SEM and TEM. Figure 2a is the SEM image of NPC without copper. In the figure, scattered carbon sheets can be observed. There are a large number of

pores on the surface of the carbon sheet, which are interspersed and connected with each other, forming a three-dimensional channel structure for ion diffusion and distribution. On the one hand, the porous structure can be used as a storage unit to store electrolytes. On the other hand, it can increase the volume expansion resistance of the electrode material during the charging and discharging processes, buffer the volume strain, and maintain the stability of the structure. Figure 2b,c shows that metal particles with a diameter of 0.1–0.3 μm are evenly distributed on the surface of the porous carbon network, forming a stress dispersion structure. The stress dispersion structure of the carbon mesh-anchored metal was further characterized by TEM.

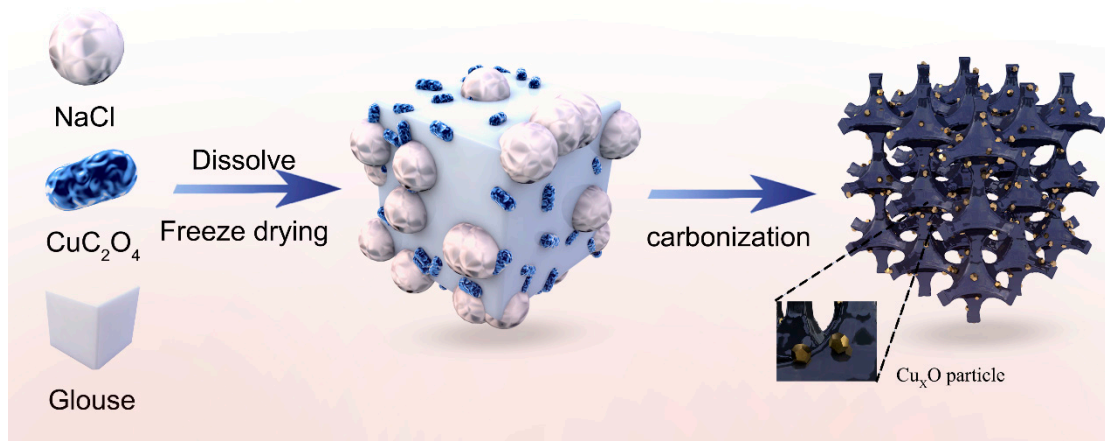


Figure 1. Schematic diagram of the Cu_xO@NPC preparation process.

According to TEM (Figure 2d), the structure, which resembles coiled paper, is carbon net. These feathery metal particles are anchored on the surface of a porous carbon net. Further magnification (Figure 2e) shows that the feathery structure is formed by the coiled lamellar layer of carbon-coated metal. Enlarge the interior (Figure 2f,g), and we can clearly distinguish the (111) crystal face from CuO, the (−111) crystal face from Cu₂O, and the (200) crystal face from Cu, which proves that the metal inside is mainly copper and its oxides. At the same time, the scanning results of elements (Figure 2h (h1–h4)) also show that the sample is mainly composed of C, N, Cu, and O elements, and the elements are evenly distributed on the surface of the sample.

Figure 2i exhibits the XRD patterns of NPC and Cu_xO@NPC. The XRD pattern corresponds to NPC and shows a wide peak near 26°, which represents the (002) crystal plane of carbon. Additionally, it shows that the peak value shifts to the high value at the low angle, which should be due to the large number of randomly oriented structures derived from the rich pore. The upwarping phenomenon of wide peaks and low-angle peaks indicates that the NPC substrate prepared belongs to hard carbon [28]. For Cu_xO@NPC, characteristic peaks belonging to Cu, Cu₂O, and CuO can be identified, which indicates that two different valence forms of copper oxides and elemental copper are distributed on the surface of the carbon network. The above discussion is consistent with the TEM characterization results. The EDS (Figure 2j) and XPS spectra (Figure 3a) also show that Cu_xO@NPC is composed of four elements: C, N, O, and Cu. EDS involves the detection and characterization of small areas, and the element content value obtained by EDS cannot accurately reflect the true element content of the whole sample. In order to determine the elemental content of C, N, O, and Cu in Cu_xO@NPC, synchronous thermal analysis (TG), nitrogen, and oxygen elemental analysis were carried out. The results are shown below. In the TG curve, it can be seen that the weight loss of the sample after 800 °C air combustion is 17.1 wt%. In this process, all the C and N inside the material are removed, and the copper is completely oxidized to CuO. Therefore, the remaining 82.9 wt% weight comes from CuO, and the atomic content of Cu can be calculated as 66.3 wt%. The nitrogen and oxygen tests show that the nitrogen atom content is 10.7 wt%, the oxygen atom content is 6.2 wt%, and the carbon

atom content is 16.8 wt% ($100 - 66.3 - 10.7 - 6.2 = 16.8$). Therefore, the content of carbon atom, oxygen atom, nitrogen atom, and copper atom in $\text{Cu}_x\text{O}@NPC$ can be calculated as 16.8 wt%, 6.2 wt%, 10.7 wt%, and 66.3 wt% (Table 1). Figure 3c shows the nitrogen adsorption/desorption curves and pore size distribution of $\text{Cu}_x\text{O}@NPC$. The specific surface area of $\text{Cu}_x\text{O}@NPC$ calculated from BET (Brunauer Emmett-Teller) is $117.4 \text{ m}^2/\text{g}$, and the pore diameter inside the carbon net is about 3 nm. The vibrational density test shows that the vibrational density of the material is $1.6 \text{ g}/\text{cm}^3$. This suggests that the addition of a porous conductive carbon network can increase the overall specific surface area of the matrix and provide abundant transmission channels, which are favorable to ions and electron shuttles. Carbon networks with high specific surface area and plentiful pore size are well recognized for their ability to supply numerous active sites, shorten ion/electron diffusion pathways, and function as stress-dispersing substrates.

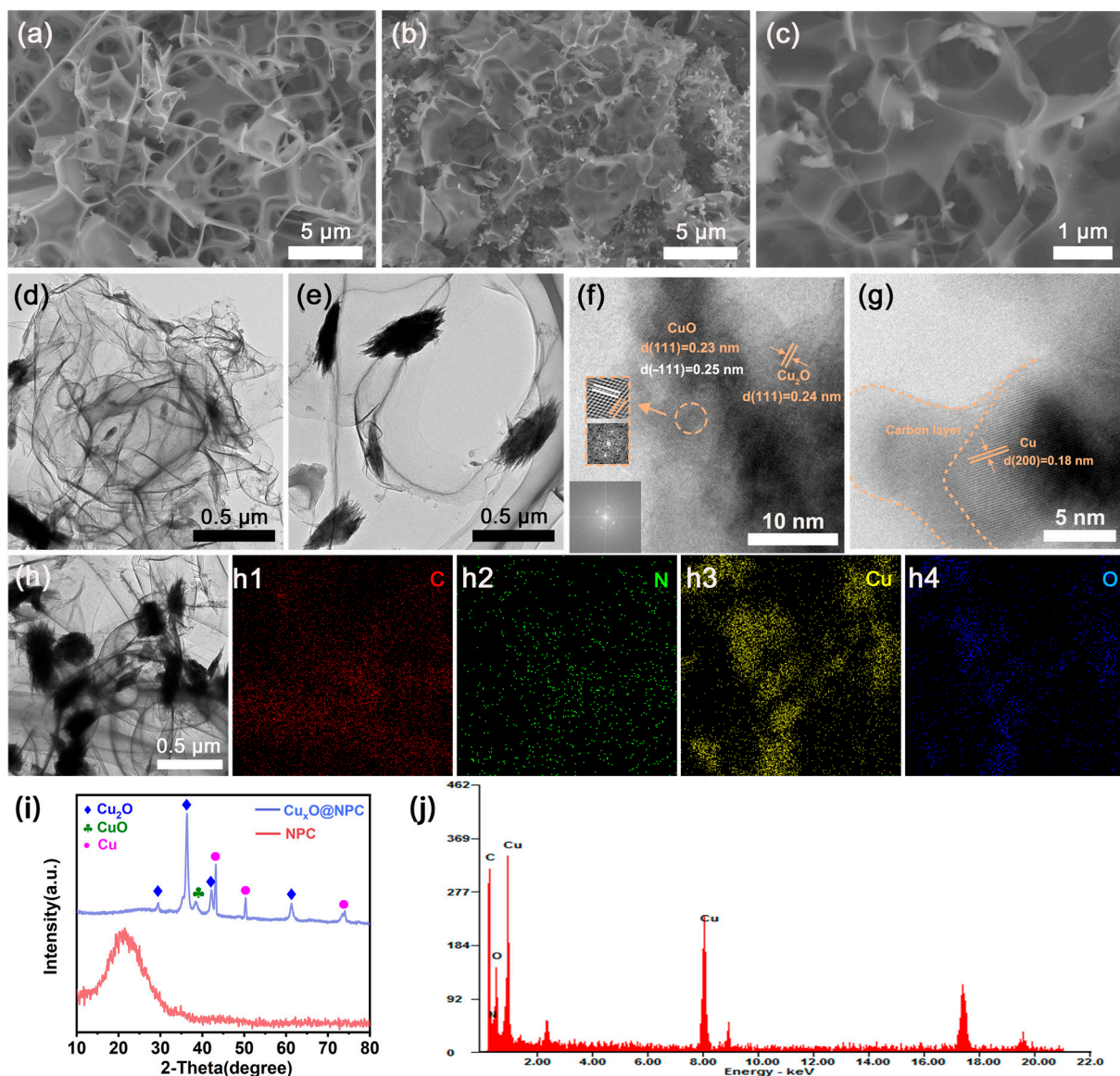


Figure 2. The microscopic morphology of NPC (a) and $\text{Cu}_x\text{O}@NPC$ (b,c) characterized by SEM with different magnifications. The microscopic morphology of $\text{Cu}_x\text{O}@NPC$ (d–h) characterized by TEM with different magnifications. The distribution of C (h1), N (h2), Cu (h3), and O (h4) elements obtained. (i) XRD patterns of NPC and $\text{Cu}_x\text{O}@NPC$. (j) Element analysis diagram obtained by EDS (energy dispersive spectrometer).

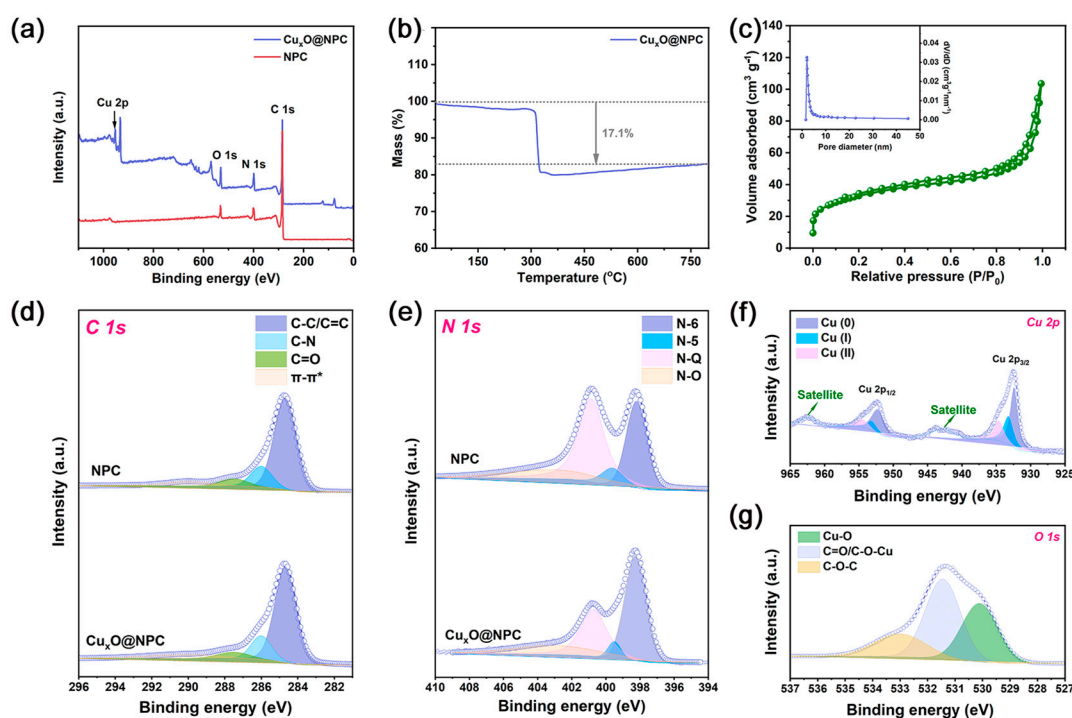


Figure 3. (a) XPS spectra of NPC and $\text{Cu}_x\text{O}@NPC$. (b) TG curve of $\text{Cu}_x\text{O}@NPC$. (c) Nitrogen adsorption/desorption curves and pore size distribution of $\text{Cu}_x\text{O}@NPC$. High-resolution C 1s (d), N 1s (e), Cu 2p (f), and O 1s (g) spectra.

Table 1. Element content percentages of C, N, O, and Cu in $\text{Cu}_x\text{O}@NPC$ obtained from synchronous thermal analysis, oxygen, nitrogen, and hydrogen analyzers.

	C (wt%)	N (wt%)	Cu (wt%)	O (wt%)
$\text{Cu}_x\text{O}@NPC$	16.8	10.7	66.3	6.2

We employ X-ray photoelectron spectroscopy (XPS) to investigate the surface composition of $\text{Cu}_x\text{O}@NPC$ further. Figure 3d–g exhibits the C 1s, N 1s, Cu 2p, and O 1s spectra for the high-resolution regions NPC and $\text{Cu}_x\text{O}@NPC$. Figure 3d shows the C 1s spectrum of NPC and $\text{Cu}_x\text{O}@NPC$, which can be divided into four independent peaks [29,30]. Among them, the peak at 284.7 eV belongs to C-C/C=C, the peak at 286.0 eV belongs to C-N, the peak at 287.5 eV belongs to C-O, and the wide peak at 290.0 eV should be derived from $\pi-\pi^*$. The peaks in Figure 3e at 398.3 eV and 399.5 eV correspond to N-6 (pyridinic N) and N-5 (pyrrolic N), and the peaks at 400.7 eV and 402.9 eV should correspond to N-Q and N-O, respectively [31]. The presence of pyridine N and pyrrole N on $\text{Cu}_x\text{O}@NPC$ proves that the presence of abundant N-doped active sites and defects in NPC effectively improves the electrochemical reactivity of the matrix, reduces the detachment of copper oxides, and significantly improves the long-term performance of the overall device [32–35]. By calculating the area percentage of each nitrogen bond peak, the percentage of different types of nitrogen can be inferred, and the results are shown in Table 1. Comparing NPC and $\text{Cu}_x\text{O}@NPC$, we can find that N-Q accounts for 43.4%, N-6 for 31.7%, and N-5 for 9.5% of non-copper-doped NPC. (Table 2) In addition, N-Q accounted for 29.2%, N-6 accounted for 46.2%, and N-5 accounted for 8.2% of copper-doped $\text{Cu}_x\text{O}@NPC$. N-Q can increase the conductivity of the base material, while N-6 and N-5 can provide active regions. This shows that the introduction of copper oxide greatly improves the reactivity of electrode materials and increases the number of electrochemically active sites. Figure 3f shows the Cu 2p spectrum of $\text{Cu}_x\text{O}@NPC$. The presence of bimodal peaks at 932.5 eV and 952.4 eV should correspond to Cu (0), while a pair of peaks at 933.2 and 953.2 eV derives from Cu

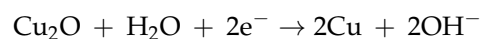
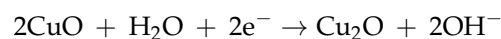
(I), and a pair of peaks at 934.6 and 954.5 eV derives from Cu (II) at Cu 2p_{3/2} and Cu 2p_{1/2} spectra in Cu_xO@NPC. In addition, a pair of peaks at 935.0 eV and 954.5 eV indicate the presence of copper oxides. In combination with XRD, Cu₂O, CuO, and Cu are present in the porous carbon network in Cu_xO@NPC [7,36,37]. The three copper-valence states have a clear division of labor: 1. CuO has a higher theoretical specific capacitance (2412 F/g); 2. Cu₂O has a higher carrier migration rate, which can accelerate ion conduction; and 3. Cu has incomparable electrical conductivity. The stress dispersion structure of various valence copper anchorings in porous carbon nets gives Cu_xO@NPC good electrochemical performance [38,39]. The O 1s spectra in Figure 3g show three peaks at 530.0, 531.3, and 532.7 eV, which should correspond to Cu-O, C=O/C-O-Cu, and C-O-C [40]. It is worth noting that the copper oxide is not simply physically loaded with the carbon matrix but is bound by a strong chemical form of the C-O-Cu bond. When the carbon net is physically combined with copper oxide, the interface bonding force is weak, and the active copper oxide is easy to fall off, resulting in lower electrode efficiency. The interfacial binding force is stronger when carbon net and copper oxide are bonded by C-O-Cu. The strong interfacial interaction of C-O-Cu can effectively fix the copper metal particles, buffer the volume effect of the electrode material, and increase structural stability [5,38].

Table 2. The XPS results of elemental doping levels of N-6, N-5, N-Q, and N-O in Cu_xO@NPC and NPC.

Samples	N-6 (%)	N-5 (%)	N-Q (%)	N-O (%)
Cu _x O@NPC	46.2	8.2	29.2	16.5
NPC	31.7	9.5	43.4	15.3

Through the above analysis, we understand the basic morphological and structural advantages of Cu_xO@NPC. Based on these, CV measurements were carried out to reflect the electrochemical mechanisms of Cu_xO@NPC and NPC. In Figure 4a, the shape of the CV curve corresponds to the NPC and is a typical rectangular shape, which indicates the capacitance mechanism of double electric layers. The CV curve for the Cu_xO@NPC electrode has obvious oxidation and reduction peaks, which represent the battery-type pseudocapacitor storage mechanism. The reduction peaks located at −0.4 V and −0.7 V represent the phase transformation from Cu (II) to Cu (I) and Cu (I) to Cu (0). The corresponding oxidation peaks located at −0.5 and −0.35 V represent the reverse process as oxidation peaks. The detailed electrochemical reaction processes are shown below:

Charge:



Discharge:



The CV results show that the energy storage mechanism of Cu_xO@NPC is a mixture of a double electric layer capacitor based on NPC and a pseudocapacitor based on copper oxides. In addition, the area of the CV curve of Cu_xO@NPC is much larger than that of NPC, which further proves the higher capacitance and electrochemical reactivity of Cu_xO@NPC. Figure 4b shows the potential-time curves of Cu_xO@NPC and NPC at a current density of 0.5 A/g with a potential range of 0.1–1 V. It can be seen that the potential-time curve of NPC is in the shape of a symmetrical triangle, indicating that NPC is an energy storage mechanism based on double-layer capacitance. On the basis of symmetry, a series of voltage platforms appear in the curve shape of Cu_xO@NPC, indicating that Cu_xO@NPC is a hybrid energy storage mechanism based on the types of double-layer

capacitor and pseudocapacitor. The voltage plateau corresponds to the occurrence of the redox reactions, which is similar to the CV discussion. In order to further explore the properties of $\text{Cu}_x\text{O@NPC}$ at different rates, CV tests (Figure 4c) were carried out at different scanning speeds. The shape of CV curves at different scanning speeds is consistent. The smaller the scanning speed, the more fully the electrolyte ion diffuses and the smaller the curve area. Redox peaks appear at the same position in all curves. Figure 4d shows the GCD curves of $\text{Cu}_x\text{O@NPC}$ at five currents from 0.5 to 7 A/g. The charge-discharge curve keeps a distinct charge-discharge platform profile even with increasing current densities, indicating the remarkable rate capability of the $\text{Cu}_x\text{O@NPC}$ electrode. Figure 4e depicts the specific capacitance calculated from GCD at different currents. Among them, $\text{Cu}_x\text{O@NPC}$ has specific capacitances of 392, 222, 147, 130, and 67 F/g at current densities of 0.5, 1, 3, 5, and 7 A/g, while NPC has specific capacitances of 209, 184, 141, 125, and 102 F/g, respectively. EIS fitting analysis was carried out with a frequency range of 100 kHz to 10 mHz for ion diffusion and electron transport of electrode materials. Figure 4f depicts the Nyquist curves, which are made up of semicircles and straight lines. $\text{Cu}_x\text{O@NPC}$ loaded with copper oxides not only has a smaller radius in the high frequency region but also has a higher slope in the low frequency region, indicating that the equivalent resistance and charge transfer resistance are obviously decreased with the introduction of copper oxides, exhibiting faster ion diffusion [41,42].

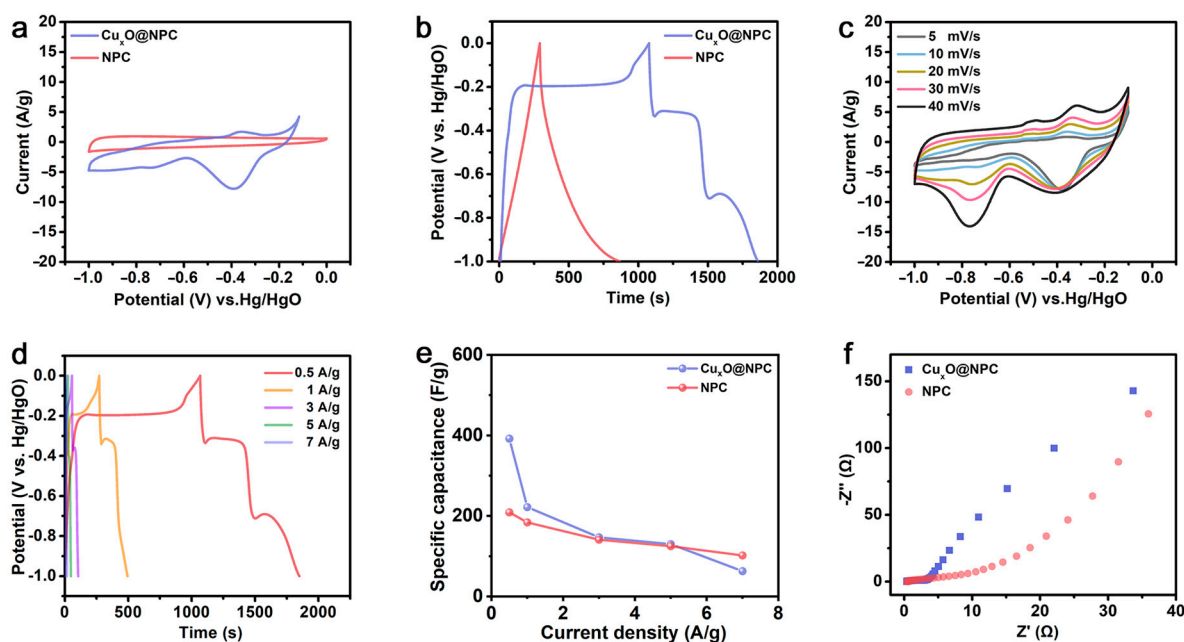


Figure 4. (a) CV curves correspond to NPC and $\text{Cu}_x\text{O@NPC}$ at a scan rate of 20 mV/s. (b) GCD curves correspond to NPC and $\text{Cu}_x\text{O@NPC}$ at 0.5 A/g. (c) CV curves correspond to NPC and $\text{Cu}_x\text{O@NPC}$ at five scan speeds. (d) Rate performance for $\text{Cu}_x\text{O@NPC}$ at five current densities. (e) Specific capacitances for NPC and $\text{Cu}_x\text{O@NPC}$ at various current densities. (f) Electrochemical impedance plots correspond to NPC and $\text{Cu}_x\text{O@NPC}$.

To further evaluate the practical application value of $\text{Cu}_x\text{O@NPC}$, an asymmetric supercapacitor device with activated carbon (AC) and $\text{Cu}_x\text{O@NPC}$ as positive and negative electrodes was assembled, and the properties of the supercapacitor were characterized. The loading mass of positive and negative active materials can be calculated using the following formula [43–45]:

$$m_1c^+v^+ = m_2c^-v^- \quad (1)$$

where, m_1 and m_2 represent the mass of positive and negative active materials, respectively. The c^+ and c^- are the values of the specific capacitances of the positive and negative electrodes, respectively. The positive and negative potential platforms are represented

by v^+ and v^- . Figure 5a presents the CV curves of two-electrode devices at different voltage ranges. With the increase of the voltage window, the CV curve would expand regularly until 0.9 V began to show signs of polarization, so we chose a voltage window of 0.0–0.8 V to evaluate its electrochemical properties. Figure 5b presents the CV curves of the device with an increasing scan speed from 5 to 40 mV/s and a voltage window controlled between 0.0 and 0.8 V. The results show that the CV curves still maintain a similar shape with increasing scanning speed without significant changes, indicating good magnification performance. The GCD curves in Figure 5c show similar platforms as the current density increases. According to Figure 5c, the specific capacitances of $\text{Cu}_x\text{O@NPC//AC}$ are 32.7, 23.3, 13.8, 8.5, and 7.7 F/g with a current density of 0.5, 1, 3, 5, and 7 A/g (Figure 5d). Surprisingly, in the cyclic stability test (Figure 5e), $\text{Cu}_x\text{O@NPC//AC}$ devices show up to 97% capacitance retention after 10,000 cycles at 5 A/g, exhibiting excellent cyclic performance. The excellent performance of the capacitor is due to the abundant three-dimensional ion diffusion channels on the electrode surface, a large number of electrochemical active sites, and highly conductive matrix materials.

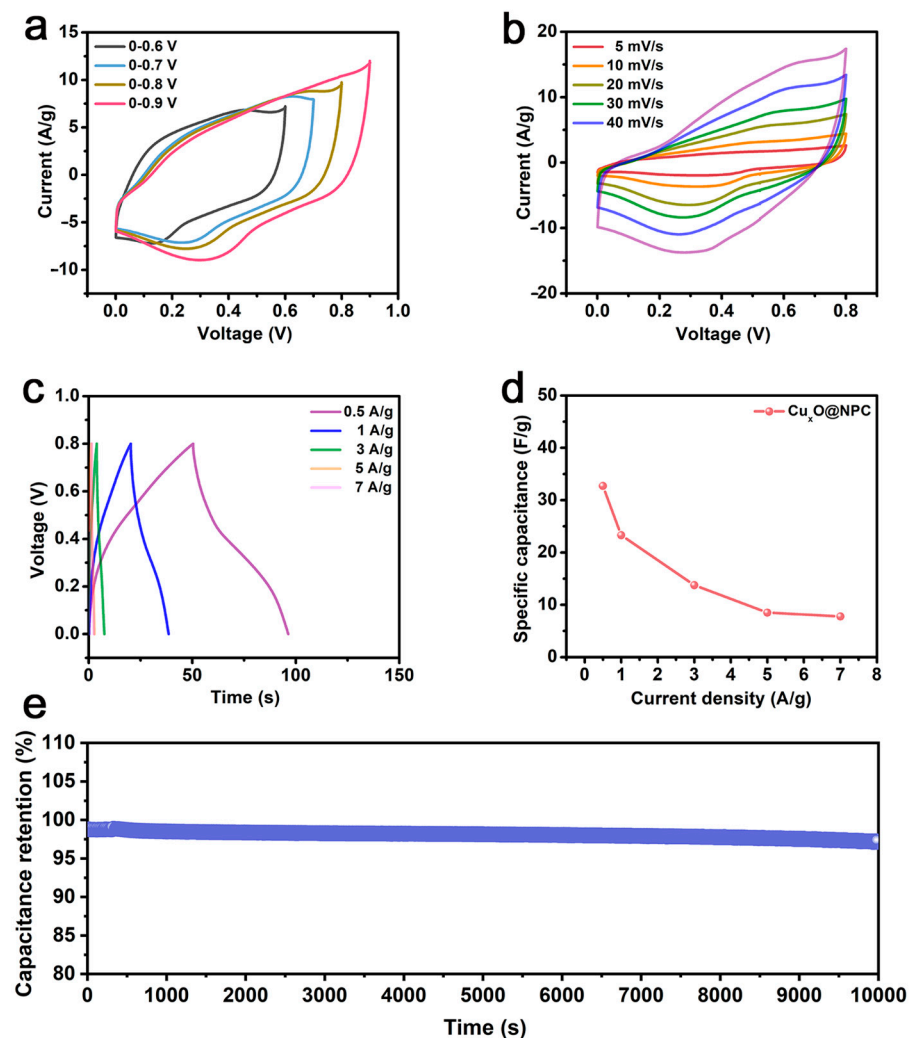


Figure 5. (a) CV curves tested at different voltage windows with a scanning rate of 30 mV/s for $\text{Cu}_x\text{O@NPC//AC}$. (b) CV curves tested at five scanning rates for $\text{Cu}_x\text{O@NPC//AC}$. (c) GCD curves of $\text{Cu}_x\text{O@NPC//AC}$ at five current densities. (d) Rate performance for $\text{Cu}_x\text{O@NPC//AC}$ at five current densities. (e) Cyclic at 5 A/g for 10,000 cycles of $\text{Cu}_x\text{O@NPC//AC}$.

4. Conclusions

In summary, copper oxides were anchored on the surface of N-doped porous carbon ($\text{Cu}_x\text{O}@NPC$) through in-situ lyophilization combined with the one-step carbonization method. Their application in supercapacitors as electrodes is studied. The feathery Cu_2O , CuO , and Cu heterostructures are uniformly anchored to the carbon conducting network, forming a stress-dispersion structure. In this stress-dispersion structure, the porous carbon network structure with a high specific surface effectively buffers the volume expansion of the electrode material occurring during the electrochemical reaction and, at the same time, allows the electrolyte to be fully infiltrated and shortens the ion diffusion path. The high content of nitrogen-doped carbon networks further increases the active sites, and together with the introduction of highly active substances such as copper oxide and cuprous oxide, the electrochemical activity of the whole material increases. The presence of copper further enhances the electrical conductivity of the whole matrix material. The composite material exhibits excellent supercapacitor properties. Specifically, the specific capacitance of $\text{Cu}_x\text{O}@NPC$ can be as high as 392 F/g (0.5 A/g) in the three-electrode system with 6 mol/L KOH as electrolyte. When applied to the two-electrode system, the cycle stability of the whole device can reach 97% after 10,000 cycles. This work not only simplifies the electrode preparation process (no conductive agent is added), but also loads the metal oxide onto the conductive network in one step. The preparation methods reported in this paper are also applicable to the preparation and application studies of other types of carbon-based metal compounds.

Author Contributions: D.L.: formal analysis, writing—review and editing, funding acquisition, and validation. H.L.: investigation and writing. Z.L.: investigation. B.L.: resources and supervision. Q.H.: conceptualization and validation. Y.W.: conceptualization and investigation. C.W.: resources and supervision. L.G.: conceptualization, resources, and supervision. All authors have read and agreed to the published version of the manuscript.

Funding: This work was financially supported by the research on safety and high-volume energy density lithium-ion battery technology (No. 50XX10XX202), the Natural Science Foundation of Shanxi Province (No. 202203021221116 and No. 20210302123067), the Program for the Innovative Talents of Higher Education Institutions of Shanxi, and the Fund Program for the Scientific Activities of Selected Returned Overseas Professionals in Shanxi Province (No. 20220012).

Data Availability Statement: Data will be made available on request.

Conflicts of Interest: The authors declare no conflict of interest.

References

1. Liu, H.; Li, D.; Liu, H.; Wang, C.; Wang, Y.; Chen, Y.; Linghu, Y.; Tian, Z.; Song, H.; Zhou, J.; et al. Devisable three-dimensional Cu_2Se nanoarrays boosts high rate Na-Ion storage. *Appl. Surf. Sci.* **2023**, *612*, 155725. [[CrossRef](#)]
2. Liu, H.; Li, D.; Liu, H.; Wang, X.; Lu, Y.; Wang, C.; Guo, L. CoSe_2 nanoparticles anchored on porous carbon network structure for efficient Na-ion storage. *J. Colloid Interface Sci.* **2023**, *634*, 864–873. [[CrossRef](#)] [[PubMed](#)]
3. Li, D.; Zhou, J.; Chen, X.; Song, H. Graphene-Loaded Bi_2Se_3 : A Conversion–Alloying-Type Anode Material for Ultrafast Gravimetric and Volumetric Na Storage. *ACS Appl. Mater. Interfaces* **2018**, *10*, 30379–30387. [[CrossRef](#)] [[PubMed](#)]
4. Li, D.; Hu, J.; Wang, C.; Guo, L.; Zhou, J. Metal-organic framework-induced edge-riched growth of layered Bi_2Se_3 towards ultrafast Na-ion storage. *J. Power Sources* **2023**, *555*, 232387. [[CrossRef](#)]
5. Li, D.; Zhou, J.; Chen, X.; Song, H. Amorphous Fe_2O_3 /Graphene Composite Nanosheets with Enhanced Electrochemical Performance for Sodium-Ion Battery. *ACS Appl. Mater. Interfaces* **2016**, *8*, 30899–30907. [[CrossRef](#)]
6. Li, D.; Zhou, J.; Chen, X.; Song, H. Achieving Ultrafast and Stable Na-Ion Storage in FeSe_2 Nanorods/Graphene Anodes by Controlling the Surface Oxide. *ACS Appl. Mater. Interfaces* **2018**, *10*, 22841–22850. [[CrossRef](#)]
7. Hu, J.-R.; Zhou, J.-W.; Jia, Y.-X.; Li, S. Cu-Modified Biomass-Derived Activated Carbons for High Performance Supercapacitors. *New Carbon Mater.* **2022**, *37*, 412–421. [[CrossRef](#)]
8. Liu, Y.; Wang, Y.; Chen, Y.; Wang, C.; Guo, L. NiCo-MOF Nanosheets Wrapping Polypyrrole Nanotubes for High-Performance Supercapacitors. *Appl. Surf. Sci.* **2020**, *507*, 145089. [[CrossRef](#)]
9. Liu, Y.; Wang, Y.; Wang, H.; Zhao, P.; Hou, H.; Guo, L. Acetylene Black Enhancing the Electrochemical Performance of NiCo-MOF Nanosheets for Supercapacitor Electrodes. *Appl. Surf. Sci.* **2019**, *492*, 455–463. [[CrossRef](#)]

10. Xu, T.; Zhang, Z.; Qu, L. Graphene-Based Fibers: Recent Advances in Preparation and Application. *Adv. Mater.* **2019**, *32*, 1901979. [[CrossRef](#)]
11. Huang, Y.; Quan, L.; Liu, T.; Chen, Q.; Cai, D.; Zhan, H. Construction of MOF-Derived Hollow Ni–Zn–Co–S Nanosword Arrays as Binder-Free Electrodes for Asymmetric Supercapacitors with High Energy Density. *Nanoscale* **2018**, *10*, 14171–14181. [[CrossRef](#)]
12. Libich, J.; Máca, J.; Vondrák, J.; Čech, O.; Sedlářková, M. Supercapacitors: Properties and Applications. *J. Energy Storage* **2018**, *17*, 224–227. [[CrossRef](#)]
13. Han, X.; Xiao, G.; Wang, Y.; Chen, X.; Duan, G.; Wu, Y.; Gong, X.; Wang, H. Design and Fabrication of Conductive Polymer Hydrogels and Their Applications in Flexible Supercapacitors. *J. Mater. Chem. A* **2020**, *8*, 23059–23095. [[CrossRef](#)]
14. Li, L.; Meng, J.; Zhang, M.; Liu, T.; Zhang, C. Recent Advances in Conductive Polymer Hydrogel Composites and Nanocomposites for Flexible Electrochemical Supercapacitors. *Chem. Commun.* **2022**, *58*, 185–207. [[CrossRef](#)]
15. Wang, J.; Li, X.; Du, X.; Wang, J.; Ma, H.; Jing, X. Polypyrrole Composites with Carbon Materials for Supercapacitors. *Chem. Pap.* **2017**, *71*, 293–316. [[CrossRef](#)]
16. Zhong, M.; Zhang, M.; Li, X. Carbon Nanomaterials and Their Composites for Supercapacitors. *Carbon Energy* **2022**, *4*, 950–985. [[CrossRef](#)]
17. Qin, F.; Tian, X.; Guo, Z.; Shen, W. Asphaltene-Based Porous Carbon Nanosheet as Electrode for Supercapacitor. *ACS Sustain. Chem. Eng.* **2018**, *6*, 15708–15719. [[CrossRef](#)]
18. Sun, Y.; Xue, J.; Dong, S.; Zhang, Y.; An, Y.; Ding, B.; Zhang, T.; Dou, H.; Zhang, X. Biomass-Derived Porous Carbon Electrodes for High-Performance Supercapacitors. *J. Mater. Sci.* **2020**, *55*, 5166–5176. [[CrossRef](#)]
19. Feng, W.; Zhang, F.; Wei, K.; Zhai, B.; Yu, C. Controlled Synthesis of Porous Carbons and their Electrochemical Performance for Supercapacitors. *Chem. Phys. Lett.* **2022**, *806*, 140066. [[CrossRef](#)]
20. Moosavifard, S.E.; Kaverlavani, S.K.; Shamsi, J.; Bakouei, A. Hierarchical Multi-Shelled Nanoporous Mixed Copper Cobalt Phosphide Hollow Microspheres as a Novel Advanced Electrode for High-Performance Asymmetric Supercapacitors. *J. Mater. Chem. A* **2017**, *5*, 18429–18433. [[CrossRef](#)]
21. Wen, T.; Wu, X.-L.; Zhang, S.; Wang, X.; Xu, A.-W. Core–Shell Carbon-Coated CuO Nanocomposites: A Highly Stable Electrode Material for Supercapacitors and Lithium-Ion Batteries. *Chem. Asian J.* **2015**, *10*, 595–601. [[CrossRef](#)]
22. Zhang, Q.; Huang, L.; Kang, S.; Yin, C.; Ma, Z.; Cui, L.; Wang, Y. CuO/Cu₂O Nanowire Arrays Grafted by Reduced Graphene Oxide: Synthesis, Characterization, and Application in Photocatalytic Reduction of CO₂. *RSC Adv.* **2017**, *7*, 43642–43647. [[CrossRef](#)]
23. Zhang, L.; Candelaria, S.L.; Tian, J.; Li, Y.; Huang, Y.-X.; Cao, G. Copper Nanocrystal Modified Activated Carbon for Supercapacitors with Enhanced Volumetric Energy and Power Density. *J. Power Sources* **2013**, *236*, 215–223. [[CrossRef](#)]
24. Li, Z.-X.; Yang, B.-L.; Zou, K.-Y.; Kong, L.; Yue, M.-L.; Duan, H.-H. Novel Porous Carbon Nanosheet Derived from a 2D Cu-MOF: Ultrahigh Porosity and Excellent Performances in the Supercapacitor Cell. *Carbon* **2019**, *144*, 540–548. [[CrossRef](#)]
25. Wang, J.; Rao, M.; Ye, C.; Qiu, Y.; Su, W.; Zheng, S.-r.; Fan, J.; Cai, S.-l.; Zhang, W.-G. Cu-MOF Derived Cu–C Nanocomposites towards High Performance Electrochemical Supercapacitors. *RSC Adv.* **2020**, *10*, 4621–4629. [[CrossRef](#)] [[PubMed](#)]
26. Sirisomboonchai, S.; Kongparakul, S.; Nueangnoraj, K.; Zhang, H.; Wei, L.; Reubroycharoen, P.; Guan, G.; Samart, C. Enhanced Electrochemical Performances with a Copper/Xylose-Based Carbon Composite Electrode. *Appl. Surf. Sci.* **2018**, *436*, 639–645. [[CrossRef](#)]
27. Zhou, Y.; Ren, J.; Xia, L.; Wu, H.; Xie, F.; Zheng, Q.; Xu, C.; Lin, D. Nitrogen-Doped Hierarchical Porous Carbon Framework Derived from Waste Pig Nails for High-Performance Supercapacitors. *ChemElectroChem* **2017**, *4*, 3181–3187. [[CrossRef](#)]
28. Muñoz-Márquez, M.Á.; Saurel, D.; Gómez-Cámer, J.L.; Casas-Cabanas, M.; Castillo-Martínez, E.; Rojo, T. Na-Ion Batteries for Large Scale Applications: A Review on Anode Materials and Solid Electrolyte Interphase Formation. *Adv. Energy Mater.* **2017**, *7*, 1700463. [[CrossRef](#)]
29. Liu, S.; Yang, B.; Zhou, J.; Song, H. Nitrogen-Rich Carbon-Onion-Constructed Nanosheets: An Ultrafast and Ultrastable Dual Anode Material for Sodium and Potassium Storage. *J. Mater. Chem. A* **2019**, *7*, 18499–18509. [[CrossRef](#)]
30. Liu, S.; Zhou, J.; Song, H. 2D Zn-Hexamine Coordination Frameworks and Their Derived N-Rich Porous Carbon Nanosheets for Ultrafast Sodium Storage. *Adv. Energy Mater.* **2018**, *8*, 1800569. [[CrossRef](#)]
31. Zhou, X.; Chen, L.; Zhang, W.; Wang, J.; Liu, Z.; Zeng, S.; Xu, R.; Wu, Y.; Ye, S.; Feng, Y.; et al. Three-Dimensional Ordered Macroporous Metal-Organic Framework Single Crystal-Derived Nitrogen-Doped Hierarchical Porous Carbon for High-Performance Potassium-Ion Batteries. *Nano Lett.* **2019**, *19*, 4965–4973. [[CrossRef](#)]
32. Liu, B.; Cao, J.; Li, J.; Li, L.; Chen, D.; Zhang, S.; Cai, D.; Han, W. Highly Conductive Co₃Se₄ Embedded in N-doped 3D Interconnected Carbonaceous Network for Enhanced Lithium and Sodium Storage. *J. Colloid Interface Sci.* **2021**, *586*, 630–639. [[CrossRef](#)]
33. Sasikala, S.P.; Huang, K.; Giroire, B.; Prabhakaran, P.; Henry, L.; Penicaud, A.; Poulin, P.; Aymonier, C. Simultaneous Graphite Exfoliation and N Doping in Supercritical Ammonia. *ACS Appl. Mater. Interfaces* **2016**, *8*, 30964–30971. [[CrossRef](#)]
34. Wang, H.; Dai, H. Strongly Coupled Inorganic–Nano-Carbon Hybrid Materials for Energy Storage. *Chem. Soc. Rev.* **2013**, *42*, 3088–3113. [[CrossRef](#)]
35. Zhang, G.; Liu, K.; Zhou, J. Cobalt Telluride/Graphene Composite Nanosheets for Excellent Gravimetric and Volumetric Na-Ion Storage. *J. Mater. Chem. A* **2018**, *6*, 6335–6343. [[CrossRef](#)]

36. Liu, S.; Yin, Y.; Hui, K.S.; Hui, K.N.; Lee, S.C.; Jun, S.C. High-Performance Flexible Quasi-Solid-State Supercapacitors Realized by Molybdenum Dioxide@Nitrogen-Doped Carbon and Copper Cobalt Sulfide Tubular Nanostructures. *Adv. Sci.* **2018**, *5*, 1800733. [[CrossRef](#)]
37. Liu, W.; Mei, J.; Liu, G.; Kou, Q.; Yi, T.; Xiao, S. Nitrogen-Doped Hierarchical Porous Carbon from Wheat Straw for Supercapacitors. *ACS Sustain. Chem. Eng.* **2018**, *6*, 11595–11605. [[CrossRef](#)]
38. Li, D.; Liu, H.; Liu, H.; Chen, Y.; Wang, C.; Guo, L. A NiCoSe_x/CG Heterostructure with Strong Interfacial Interaction Showing Rapid Diffusion Kinetics as a Flexible Anode for High-Rate Sodium Storage. *Dalton Trans.* **2023**, *52*, 5192–5201. [[CrossRef](#)]
39. Liu, C.; Huang, Q.; Zheng, K.; Qin, J.; Zhou, D.; Wang, J. Impact of Lithium Salts on the Combustion Characteristics of Electrolyte Under Diverse Pressures. *Energies* **2020**, *13*, 5373. [[CrossRef](#)]
40. Arkhipova, E.A.; Ivanov, A.S.; Maslakov, K.I.; Savilov, S.V. Nitrogen Doping of Mesoporous Graphene Nanoflakes as a Way to Enhance Their Electrochemical Performance in Ionic Liquid-Based Supercapacitors. *J. Energy Storage* **2020**, *30*, 101464. [[CrossRef](#)]
41. Liu, C.; Xu, D.; Weng, J.; Zhou, S.; Li, W.; Wan, Y.; Jiang, S.; Zhou, D.; Wang, J.; Huang, Q. Phase Change Materials Application in Battery Thermal Management System: A Review. *Materials* **2020**, *13*, 4622. [[CrossRef](#)] [[PubMed](#)]
42. Zhang, Z.; Lin, J.; Hao, J.; Xue, F.; Gu, Y.; Zhu, Z.; Li, Q. Exploration of Fast Ion Diffusion Kinetics in Graphene Nanoscrolls Encapsulated CoSe₂ as Advanced Anode for High-Rate Sodium-Ion Batteries. *Carbon* **2021**, *181*, 69–78. [[CrossRef](#)]
43. Xu, D.; Huang, G.; Guo, L.; Chen, Y.; Ding, C.; Liu, C. Enhancement of Catalytic Combustion and Thermolysis for Treating Polyethylene Plastic Waste. *Adv. Compos. Hybrid Mater.* **2022**, *5*, 113–129. [[CrossRef](#)]
44. Zhang, Y.; Duan, S.; Li, Y.; Zhang, S.; Wu, Y.; Ma, M.; Tao, C.; Zhang, Z.; Qin, D.; Xie, E. 2.6 V Aqueous Symmetric Supercapacitors Based on Phosphorus-Doped TiO₂ Nanotube Arrays. *Dalton Trans.* **2020**, *49*, 1785–1793. [[CrossRef](#)] [[PubMed](#)]
45. Qin, J.; Liu, C.; Huang, Q. Simulation on Fire Emergency Evacuation in Special Subway Station Based on Pathfinder. *Case Stud. Therm. Eng.* **2020**, *21*, 100677. [[CrossRef](#)]

Disclaimer/Publisher's Note: The statements, opinions and data contained in all publications are solely those of the individual author(s) and contributor(s) and not of MDPI and/or the editor(s). MDPI and/or the editor(s) disclaim responsibility for any injury to people or property resulting from any ideas, methods, instructions or products referred to in the content.